Chiral magnetic excitations in FeGe films

Emrah Turgut,[1] Albert Park,[1] Kayla Nguyen,[1] Austin Moehle,[1] David A. Muller,[1,2] and Gregory D. Fuchs[1,2,*]

[1]*School of Applied and Engineering Physics, Cornell University, Ithaca, New York 14853, USA*

[2]*Kavli Institute at Cornell for Nanoscale Science, Ithaca, New York 14853, USA*

(Received 11 August 2016; revised manuscript received 20 February 2017; published 12 April 2017)

Although chiral magnetic materials have emerged as a potential ingredient in future spintronic memory devices, there are few comprehensive studies of magnetic properties in scalably grown thin films. We present growth, systematic physical and magnetic characterization, and microwave absorption spectroscopy of B20 FeGe thin films. We also perform micromagnetic simulations and apply analytical theory to understand the dynamical magnetic behavior of this material. We find magnetic resonance features in both the helical and field-polarized magnetic states, which are well explained by micromagnetic simulations and analytical calculations. In particular, we show the resonant enhancement of spin waves along the FeGe film thickness that has a wave vector matching the helical vector. Using our analytic model, we also describe the resonance frequency of a helical magnetic state in bulk materials and thin films, which depends strongly on its untwisting field. Our results pave the way for understanding and manipulating high frequency spin waves in thin-film chiral magnet FeGe near room temperature.

DOI: 10.1103/PhysRevB.95.134416

I. INTRODUCTION

Understanding the static and dynamic magnetic properties of materials is a key to their incorporation in active spintronic devices. In light of the recent proposals for power-efficient spintronic memory devices based in chiral magnetism [1,2], it is increasingly important to characterize chiral magnetic materials in scalably grown thin-film form. Although the resonant spin dynamics in chiral magnetic films are more complex than conventional ferromagnetic resonance in uniformly magnetized ferromagnetic films, understanding and measuring chiral magnetic excitations enable physical insight into the magnetic states of these materials and offer quantitative characterization of dynamical properties that are relevant to future magnetic technologies.

The noncollinear spin texture that appears in chiral magnets is a consequence of the Dzyaloshinskii-Moriya interaction (DMI), which presents at interfaces and in the volume of noncentrosymmetric materials with broken inversion symmetry [3–6]. One class in these materials is cubic B20 crystalline monosilicides and monogermanides of transition magnetic elements, e.g., MnSi, FeCoSi, and FeGe [7]. Although they are in the same symmetry group, these silicides and germanides have surprising and distinctive electronic and magnetic properties, depending on pressure, temperature, electric, and magnetic fields [8–11].

Among B20 compounds, FeGe has the highest critical temperature, 278 K, for ordered chiral spin textures [7,12]. FeGe also has -0.6% lattice mismatch with the Si [111] surface, enabling scalable thin-film growth [13,14], particularly in comparison with the mismatch of -3% and -6% for MnSi and FeCoSi, respectively [15,16]. Furthermore, in recent computational studies [17,18], thin film and nanoscale confinement of FeGe has been shown to stabilize the creation of a magnetic skyrmion, a two-dimensional chiral spin texture with nontrivial topological order. These properties also make FeGe thin films attractive for emerging spintronic applications with chiral magnets.

Although B20 FeGe thin films have been the subject of intense theoretical and computational studies, experimental studies have been limited to reports of the topological Hall effect and polarized neutron scattering measurements [13,14,19–23]. Furthermore, recent Lorentz transmission electron microscopy (TEM) and transport studies of FeGe and MnSi thin films have questioned the common interpretation of the topological Hall effect as arising solely from a skyrmion lattice phase [13,19,24,25]. These studies point out that transport measurements of B20 films are hard to interpret unambiguously because electron skew scattering by complex helical spin structures also contributes a Hall effect signal [13,26]. These difficulties motivate the application of alternative characterization methods to help identify chiral magnetic states and to quantify magnetic behavior in thin-film materials.

Microwave absorption spectroscopy (MAS) is a powerful tool used to probe magnetization in both conventional ferromagnetic and complex materials [27–30]. In MAS, resonant absorption of a microwave magnetic field depends on the magnetic properties and configuration. For example, ferromagnetic resonance has been used to characterize effective magnetization, the damping parameter, and even magnetic anisotropies [31,32]. Moreover, MAS has been used to show universality of helimagnon and skyrmion excitations in bulk B20s regardless of being a conductor or an insulator [33]. Microwave fields are useful not only for understanding chiral magnets, but they can also create a giant spin-motive force in chiral magnets [34,35].

Here we report an experimental, theoretical, and micromagnetic study of chiral magnetic excitations in FeGe thin films by waveguide MAS. First, we describe the growth of B20 crystalline thin FeGe films via magnetron sputtering and systematic characterization of their physical and magnetic properties by x-ray diffraction, electron backscattering diffraction (EBSD), and magnetometry. Then, using parameters extracted directly from magnetic characterization, we study spin wave and resonant excitations in the helical and field-polarized states using micromagnetic simulations. With this framework being used to understand resonance frequencies and spin-wave modes, we experimentally perform temperature and magnetic field dependent MAS. We find that although the field-polarized

*Corresponding author: gdf9@cornell.edu

magnetic resonance can be described by Kittel's formula, the helical state magnetic dynamics are more complex. In particular, an important mode occurs when spin waves are excited along the film thickness with a wavelength that matches the helical period. In addition, we theoretically calculate the resonant frequencies of the helicoids and find that it depends strongly on the value of the critical magnetic field that unwraps helicoid into the field-polarized spin state.

This paper is organized as follows. In Sec. II, we describe the growth and characterization of the FeGe film. We report magnetometry studies in Sec. III and present micromagnetic simulations in Sec. IV. Then, we discuss experimental measurements of MAS in Sec. V. We analytically calculate resonance dynamics in helical magnet in Sec. VI. Finally, we conclude in Sec. VII.

II. FILM GROWTH AND CHARACTERIZATION

FeGe thin films are co-sputtered from Fe and Ge targets onto the surface of undoped Si [111] wafers and annealed post-growth at 350 °C for 30 minutes to create the B20 crystalline phase. The films are then characterized by x-ray diffraction, TEM, and EBSD. The thickness of the film we studied is 176 nm, which was determined by cross sectional imaging with a scanning electron microscope (see the Supplemental Material [36]).

In Fig. 1(a), we first present our x-ray diffraction measurements of the film using a Bruker General Area Detector Diffraction System, which produces a wide range of θ and χ angles in one measurement, enabling a survey of the crystal properties. The presence of sharp peaks instead of rings indicates both good crystallinity and epitaxy of the FeGe film with the underlying Si substrate. Next, to quantify crystal properties more carefully, we acquire $\theta - 2\theta$ measurements of the film using a Rigaku SmartLab x-ray diffractometer. In Fig. 1(b), we first plot the x-ray $\theta - 2\theta$ measurement at $\chi = 0^\circ$, i.e., the film plane is placed perpendicular to the x-ray incidence plane. From the diffraction peak of FeGe [111], we first find that the spacing between the atomic layers d_{111} along the [111]-out-of-plane (OOP) direction is 2.7045 $\pm$ 0.0001 Å. This value is calibrated against the known lattice constant of the Si substrate, 5.431 Å [37]. The diagonal length of the FeGe unit cell along the [111] axis is then found as $3d_{111} = 8.1135 \pm 0.0003$ Å, which is 0.32% shorter than the bulk value of 8.13977 Å [38]. Secondly, we measure x-ray diffraction of the [400] lattice spacing of both Si and FeGe at $\chi = 54.74^\circ$. Initially, we find the Si [400] peak and calibrate the instrument again by the known Si lattice constant, then rotate the angle ϕ by 30° and perform the $\theta - 2\theta$ scan for the FeGe [400] peak [Fig. 1(c)]. By fitting the FeGe [400] peak, we find the spacing $d_{400} = 1.1777 \pm 0.0002$ Å. Previous studies reported a slight distortion of the cubic unit cell to a rhombohedral unit cell in MnSi films grown on Si [111] [37,39]; we observe a qualitatively similar effect in FeGe. By using the calculated lattice spacing $d_{111} = 2.7045$ Å and $d_{400} = 1.1777$ Å of FeGe from Figs. 1(b) and 1(c) and the rhombohedral lattice spacing formula from Ref. [40] (see also the Supplemental Material [36]), we find that the angle, the lattice constant, and the longer diagonal length of the rhombohedral unit cell are 89.678°, 4.7109 Å, and 8.2053 Å, respectively [Fig. 1(d)]. As a result, our films have −0.32% compressive strain along the [111] OOP axis and 0.8% tensile strain in the plane. This large in-plane (IP) tensile strain in a thick film is surprising because the lattice mismatch between Si and bulk FeGe is only 0.08%—which is 10 times smaller than our observation. In addition, our $\epsilon_\perp = -0.0032$ compressive and $\epsilon_\parallel = 0.008$ tensile strains and previous $\epsilon_\perp$ reports in FeGe films [13,14,23] are very similar to the strains measured in MnSi thin films [37,39], even though FeGe has a 40 times closer lattice match with the Si [111] substrate than with MnSi [41]. Indeed, MnSi films that are as thick as our film have been recently shown to release the substrate stress [42], which suggests differences between the two B20 systems and which will require further investigation.

To understand induced stress and magnetic anisotropy in our films, we analyze the measured strains and model the distortion of the FeGe unit cell from a cubic to a rhombohedral shape. This distortion is characterized by the ratio $\epsilon_\perp/2\epsilon_\parallel$, which we calculate as −0.2 using the values above. This ratio can be also theoretically calculated by the elastic constants of FeGe using $\frac{\epsilon_\perp}{2\epsilon_\parallel} = -\frac{3\kappa-2c_{44}}{3\kappa+4c_{44}}$, where κ is the bulk modulus and c_{44} is the shear modulus [37,43]. The theoretical expectation for this ratio is −0.18, which is in very close agreement with our experimentally measured value. Karhu *et al.* also reported a slightly larger value for MnSi films for thinner films, which was attributed to softening of c_{44} values in the thin films [37]. Furthermore, using the derivation in Ref. [43] and above strains, we calculate the lateral and the perpendicular stress in FeGe as 2.6 GPa and 5.0 GPa, respectively (see the Supplemental Material [36]). Recent papers on single-crystal bulk MnSi indicated that a change in the uniaxial magnetic anisotropy and a collapse of the stable skyrmion phase were induced by applying ∼100 MPa stress along the [111] axis. In contrast, the helical phase was robust to such stresses [44,45]. Although a complete understanding of the magnetic phase diagram of thin film FeGe under stress requires more comprehensive experimental and theoretical study, our analysis suggests that the stress-induced rhombohedral distortion creates uniaxial–easy plane anisotropy in the film and facilitates the helical and field polarized states in our films. This conclusion is consistent with the magnetometry measurements presented in the next section and with previous studies on B20 thin films [13,15,19,21,26].

Next we characterize the FeGe grains using plane-view TEM and EBSD. The transmission electron micrograph shown in Fig. 1(e) was taken using a Tecnai-F20 at 200 kV electron energy. It shows that our films have both ordered and disordered grains. We further investigate the nanoscale crystal configuration of the grains with EBSD [Figs. 1(f)–1(i)]. The top image in Fig. 1(f) shows the scanning electron micrograph of an $8 \times 4\,\mu m^2$ region of the sample. The second EBSD micrograph [Fig. 1(g)] shows a crystalline phase map of the same region, confirming that 99% of the grains have the B20 phase. In addition, we show the EBSD crystalline orientation map along the OOP orientation [Fig. 1(h)]. The inverse pole figure map next to the EBSD map shows the crystallographic coordinate system. The grains marked with blue color are aligned with the Si [111] orientation [Fig. 1(h)], showing the high degree of alignment in agreement with the x-ray

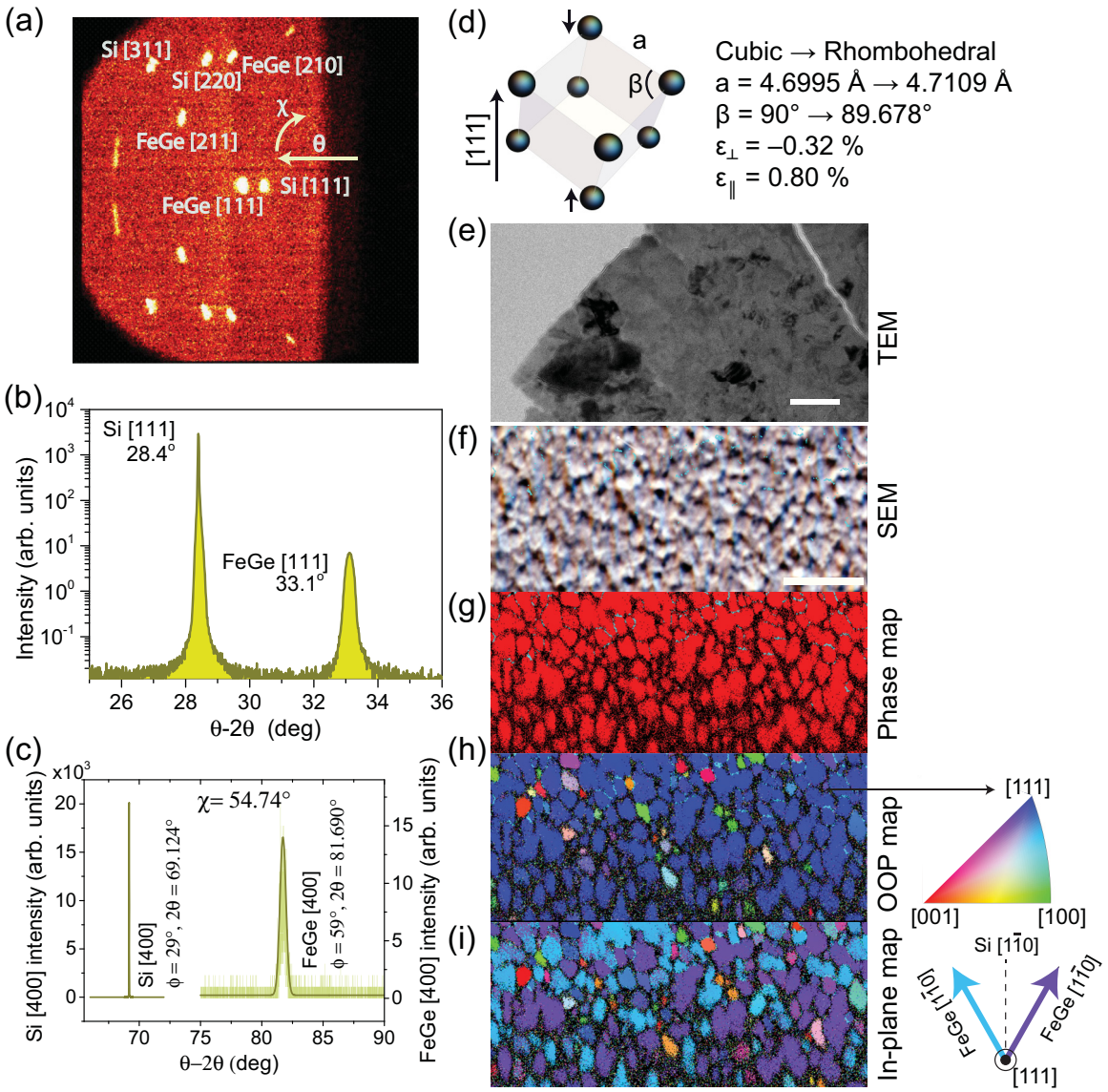

FIG. 1. X-ray and electron diffraction characterizations and transmission electron micrograph of FeGe thin film. (a) X-ray diffraction measurements made with an area detector to include χ angle profile. The presence of sharp peaks instead of rings indicates a high degree of epitaxy of FeGe film with the underlying Si substrate. The θ-2θ scan of x-ray diffraction at $\chi = 0^\circ$ (b) and $\chi = 54.74^\circ$ (c). (d) Illustration of the deformation of FeGe unit cell from a cubic to a rhombohedral and resulting lattice parameters of the rhombohedral unit cell and strains. (e) Transmission electron micrograph of plain view of the film (scale bar is 100 nm). (f) Scanning electron micrograph. (g) Crystalline phase map of the same region, with red color indicating >99% B20 phase. (h) The EBSD map along OOP. The color map next to the EBSD map shows the crystallographic coordinate system. (i) In-plane alignment of the grains. The light blue and purple colors show twinned grains with respect to Si[1$\bar{1}$0] orientation. The scale bar is 2 μm through (f)–(i).

diffraction data. Our IP orientation analysis of grains [Fig. 1(i)] shows twinning of the FeGe grains with light blue and purple colors, in which the FeGe [1$\bar{1}$0] orientation is rotated either $+30^\circ$ or -30° in the plane with respect Si[1$\bar{1}$0] orientation. These high-quality polycrystalline films with grain sizes larger than the helical lattice constant of FeGe (70 nm) [46] allow us to study chiral magnetism in B20 thin-film materials.

III. MAGNETIC PROPERTIES

In this section, we characterize the magnetic properties of our FeGe thin films. First, we measure the magnetic moment of our film as a function of an external magnetic field, H, and temperature, T, using a vibrating sample magnetometer (VSM). Our films have an easy-plane magnetic anisotropy evidenced by an OOP magnetic saturation field that is four times larger than the saturation in the plane, as shown in Figs. 2(a) and 2(b). Additionally, we find that as the temperature decreases, the magnetic moment and the saturation magnetic field increases. We note that while the OOP magnetic moment curves do not indicate an obvious magnetic phase change, the IP magnetization curves have a feature around 400 Oe that does not appear in the typical magnetic hysteresis of a conventional ferromagnetic material.

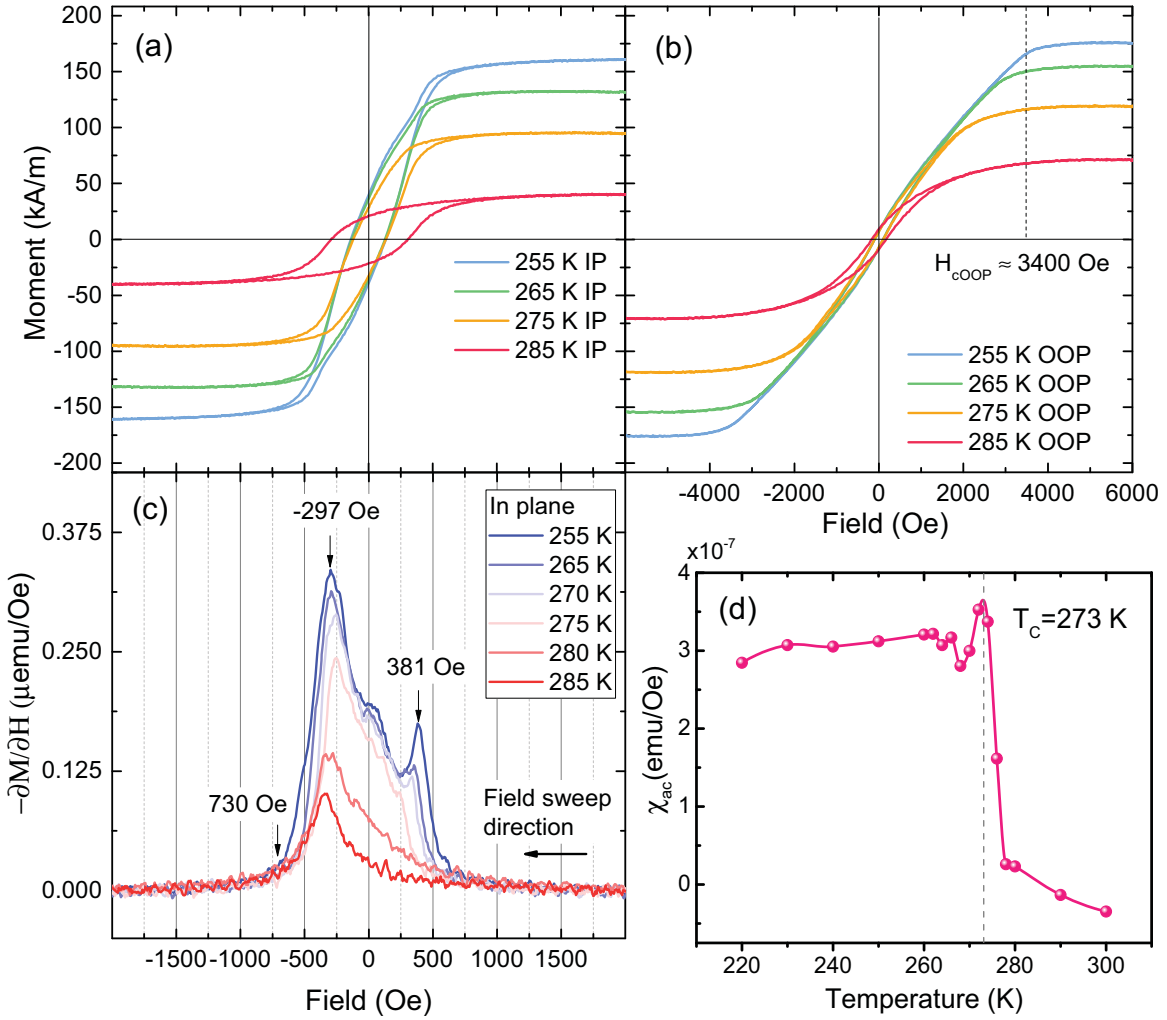

FIG. 2. Magnetometry measurements of our thin film FeGe. (a) *M-H* curves for the in-plane (IP) and (b) for the OOP fields. (c) The derivative of the IP magnetization with respect to the applied magnetic field to better reveal unwinding of the helical phase. (d) The ac magnetic susceptibility with 20 Oe dc and 10 Oe ac field in the plane.

To better reveal the features, we plot the derivative of the IP magnetization with respect to the applied magnetic field in Fig. 2(c). As we decrease the magnetic field from the large positive values at $T = 255$ K, there is a peak at $H = 381$ Oe, where the field polarized state wraps into a helical state. As we continue, there is another peak at $H = -297$ Oe, where the helix unwraps again into the field polarized state. We interpret these fields as the center of a broad wrapping/unwrapping range, not as a sharp phase boundary. In this scenario, both the helical and field polarized states can coexist around these fields. Broadening of the wrapping/unwrapping fields is likely due to inhomogeneities in the film thickness and film anisotropy and is consistent with previous studies of B20 MnSi thin films [21]. From Fig. 2(c), we also find the saturation field at $H = 730$ Oe, where the susceptibility at all temperatures converge and approach zero for the IP geometry. The saturation field for the OOP geometry is found as $H_{cOOP} = 3400$ Oe in Fig. 2(b), which we will use to determine the easy plane anisotropy for the micromagnetic simulations and the analytic calculations in the following sections.

To identify the transition temperature of our FeGe films, we measure the ac magnetic susceptibility in a 20 Oe dc bias field with ac fields, which has a 10 Oe amplitude, as a function of T [Fig. 2(d)]. The emergence of a peak at the critical temperature (T_c) 273 K indicates a magnetic phase transition, which is evidence of a transition from an OOP q-axis helical phase to a paramagnetic phase or a precursor region. This conclusion is also consistent with the data presented in the following sections and previous polarized neutron scattering studies in FeGe and MnSi thin films [19,21].

IV. MICROMAGNETIC SIMULATIONS

In this section, to identify the spin dynamics in FeGe thin films, we perform micromagnetic simulations using the Mumax3 software [47]. We identify the magnetic properties of the film as simulation parameter inputs using magnetometry measurements in Fig. 2 and the following relations: $H_k = \frac{\pi^2}{16} H_d$, where $H_k = 450$ Oe is the untwisting field and $H_d = 730$ Oe is the saturation field that is extracted from the dM/dH curve in Fig. 2(c). The saturation field in chiral magnets

is described by $H_d = \frac{D^2}{2AM_s} = \frac{8\pi^2 A}{L_D^2 M_s}$, where D is the DMI constant, A is the exchange constant, M_s is the saturation magnetization, and $L_D = 70$ nm is the helical period [21,24,34,48]. We find that M_s is 150 kA/m from Fig. 2(a) by interpolating the $T = 255$ K and $T = 265$ K curves to $T = 258$ K, which is the temperature of the resonance experiment in the next section. Then, we find that A and D are 6.8×10^{-13} J/m and 0.12 mJ/m^2, respectively. We also assume that the helical period L_D does not depend on the saturation magnetization or temperature [21]. Finally, we calculate the uniaxial anisotropy to be -3.5 kJ/m^3 using $H_{cOOP} = 3400$ Oe and eq. (6) from Ref. [39] (see the Supplemental Material [36] for details). We note that the determination of the uniaxial anisotropy has a large uncertainty due to the large variation of the magnetic properties near the critical temperature [49].

In the simulation, the sample dimension is $3.2 \times 3.2 \times 176$ nm^3 in the x, y, and z directions, and the unit cell is a $0.8 \times 0.8 \times 0.8$ nm^3 cube. We apply 16 repetitive periodic boundary conditions in the x and y directions to mimic the uniform film. Furthermore, we study chiral dynamics at $T = 0$ K, meaning we did not implement a fluctuating thermal field, which is necessary to quantitatively capture phase transitions between the helix and the field-polarized states. Thus, we supply this information to the simulation by initializing the magnetic states based on experimental magnetometry results. As a result of this initialization, our simulation does not account for the resonance dynamics of mixed helical and field-polarized states; however, it does allow us to identify resonance dynamics of each state separately.

In micromagnetic simulations, we use the ringdown method to obtain dynamic properties. We first initialize the system in the helical state between -500 Oe and 500 Oe and the field-polarized state for the rest of the magnetic fields. Then, for each field, we relax the system to its equilibrium state, where all torques vanish. For example, in Figs. 3(b)–3(d), we show these equilibrium spin configurations at $H = 1750$ Oe, 250 Oe, and 0 Oe applied IP fields. Next, we apply a magnetic pulse with a Gaussian profile and record the x, y, and z components of the local magnetic moments at 25 ps time steps for a 20 ns duration (see the Supplemental Material [36] for details). The Gilbert damping parameter is set to an artificially small value ($\alpha = 0.002$) to capture enough periods of the natural oscillations so that we can identify the modes that are sustained by microwave driving [50,51]. We note that this small value will result in an artificially narrow resonance frequency relative to the experiment. To be consistent with the coordinate system we use for theoretical calculations in Sec. VI, we also perform a coordinate transformation of the magnetization components from Cartesian coordinates into spherical coordinates. The z component of magnetization simply becomes θ, whereas the azimuthal angle φ is calculated from the x and y components in the plane.

To calculate the natural modes and frequencies, we compute the discrete Fourier transform of the local magnetic deviation from equilibrium for each magnetic field. Because the deviation in both θ and φ angles results in the same resonance frequencies and modes, we plot only θ in Fig. 3. Next, we compute spatially averaged Fourier coefficients of all spins to obtain the power spectral density (PSD) [51]. Figure 3(a) shows the PSD for frequencies between 0.5 and 7 GHz and IP H between -2000 Oe and 2000 Oe. We identify three magnetic fields ($H = 1750$ Oe, 250 Oe, and 0 Oe) to explore the resonance behavior and modes. We also define wrapping number ς, which is $(\varphi_N - \varphi_1)/2\pi$ total wrapping of spins at the equilibrium configuration. To reveal the modes, we plot the Fourier coefficients as a function of the frequency

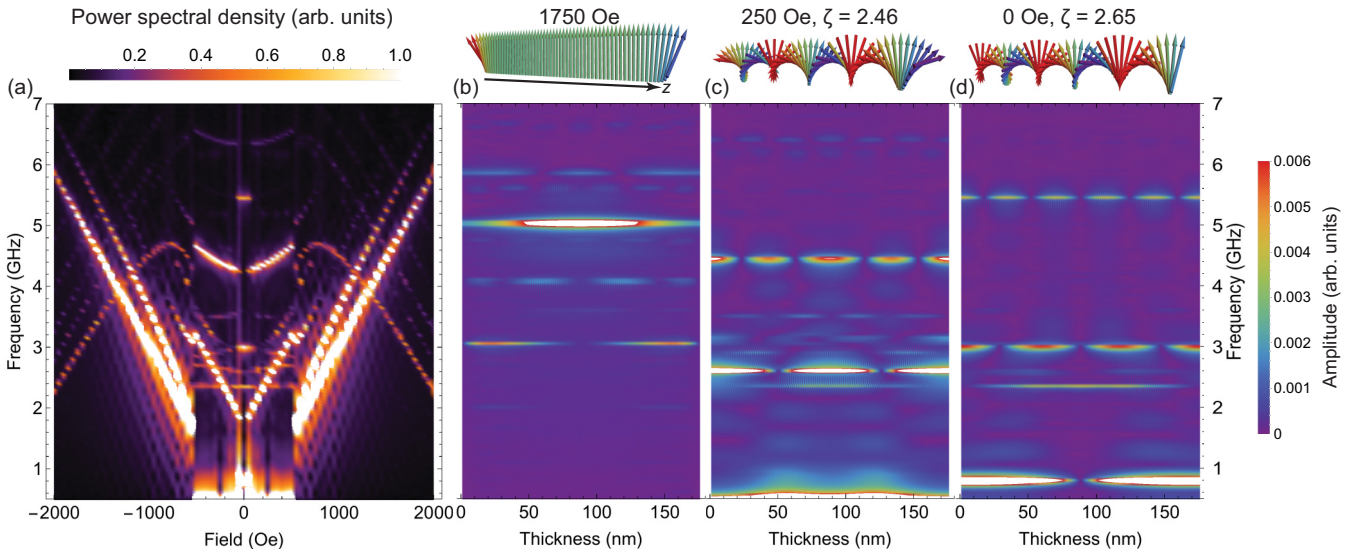

FIG. 3. The PSD and natural oscillation modes of spin waves. (a) The PSD of spatially summed Fourier coefficients as a function of the in-plane magnetic field. The helical spin configuration presents between -500 Oe and 500 Oe, and the field-polarized state presents for $H >$ 500 Oe and $H < -500$ fields. (b)–(d) The variation of spins from the equilibrium condition as a function of film thickness and the resonance frequency. (b) At $H_x = 1750$ Oe field, the field-polarized state has a Kittel-type uniform mode. (c) At $H_x = 250$ Oe field, the helical state resonance with the wrapping number ζ is 2.46, which allows only even nodes (0, 2, and 4). (d) At $H_x = 0$ Oe field, the helical state resonance with the wrapping number ζ is 2.65, which allows only odd nodes (1, 3, and 5).

and thickness (z direction) in Figs. 3(b)–3(d), with the spin configurations along the thickness shown above each plot.

The first region is at $H = 1750$ Oe, where we observe a Kittel-type uniform resonance of the field-polarized state at 5 GHz [Fig. 3(d)]. There are also edge modes that are inversely proportional to the magnetic field at 3 GHz. The second region is at $H = 250$ Oe, where the wrapping number of the helical state is $\varsigma = 2.46$. The resonance frequencies are located at 4.5 GHz, 2.6 GHz, and 0.5 GHz, and the corresponding number of nodes are 4, 2, and 0, with only even numbers because $2\varsigma = 4.9 < 5$. On the other hand, in the third region at $H = 0$ Oe, the system is driven into $\varsigma = 2.65$ times wrapping, which is slightly larger than the expected 2.51 (176 nm/70 nm) because of the demagnetizing field of the film and the absence of an external field. The resonance frequencies then increase to 5.5 GHz, 3.0 GHz, and 0.8 GHz, and the number of nodes becomes odd—5, 3, and 1, respectively, because $2\varsigma = 5.3 > 5$. These results show that spin waves in chiral B20 thin films are sensitive to helical wrapping—constrained by both the thickness and the discrete wrapping number.

V. EXPERIMENT: MAS

After we account for spin waves in the helical and field-polarized states, we experimentally perform magnetic resonance measurements by placing FeGe film on a broadband metallic coplanar waveguide (CPW). More details about the design and characteristics of the CPW can be found in Ref. [52]. We apply a radio frequency (RF) field with a signal generator and monitor the transmitted power with an RF diode as a function of magnetic field and temperature. To remove any nonmagnetic signals, we lock-in to the transmitted RF power referenced a magnetic field modulation that we introduce using an ac field coil. Thus, we measure the derivative of the transmitted power, $\partial P/\partial H \sim \Delta P/H_{ac}$, as shown in Fig. 4. For each temperature, we vary the microwave frequency from 0.5 GHz to 7 GHz with a 0.25 GHz step size and H from 3000 Oe to −3000 Oe with a 30 Oe step size. The temperature of the sample is controlled by a Peltier element that allows a temperature control between $T = 300$ K and 255 K.

In Figs. 4(a)–4(c), we plot the microwave absorption spectra at $T = 283$ K, $T = 273.5$ K, and $T = 258$ K, respectively (data for the full temperature range can be found in the Supplemental Material [36]). At $T = 283$ K, the film is in a paramagnetic state, and it shows hardly any microwave absorption [Fig. 4(a)]. At $T = 273.5$ K, which is slightly higher than the critical temperature ($T_c = 273$ K) but lower than the Curie temperature (278 K) [49], it shows a field-polarized magnetic resonance [Fig. 4(b)]. After we further decrease the temperature below T_c to $T = 258$ K, we find an

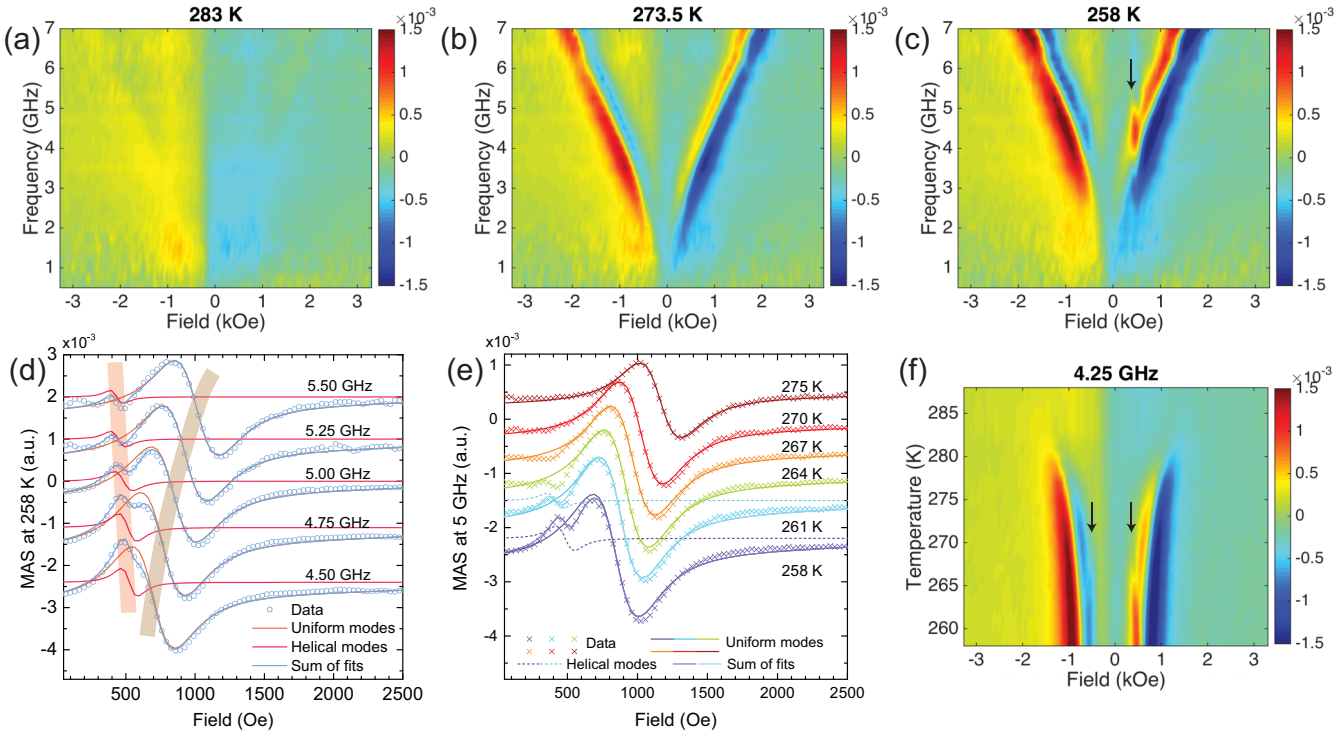

FIG. 4. Experimental measurements of MAS of the FeGe film at different temperature, in-plane magnetic field, and microwave frequency. (a) The MAS at temperature $T = 283$ K, showing no clear absorption feature in the paramagnetic phase. (b) The MAS slightly above the critical temperature (273.5 K > 273 K), which has only the field-polarized state resonance. (c) The MAS below the critical temperature, which has both the helical (arrow) and the field polarized resonances. (d) The MAS linecuts from (c) through 4.5–5.5 GHz frequencies. Additional Lorentzian lineshape derivatives shown by the red curves at around the untwisting field indicate the helical resonance. While the uniform mode follows Kittel's formula (thick brown line), the helical resonance field is relatively constant through the different frequencies (thick red line). (e) The MAS linecuts at 5 GHz and different temperatures. The helical mode shown by the dotted curves can be fitted by a derivative of Lorentzian lineshape at 261 and 258 K temperatures. (f) The MAS at 4.25 GHz as the field and the temperature vary. Both $H < 0$ and $H > 0$ show the helical resonance indicated by arrows.

additional resonance in our FeGe film near the untwisting magnetic field [Fig. 4(c)]. In the following, we investigate these two resonances further to understand their nature.

The first resonance is a Kittel-type uniform magnetic resonance of the field-polarized state. We fit the absorption spectra to a derivative of Lorentzian lineshape to extract the resonance fields, frequencies f, and the linewidths ΔH (see the Supplemental Material [36]). Linewidths are proportional to the resonance frequencies by $\Delta H = \Delta H_0 + \frac{4\pi\alpha f}{\gamma_e}$, where γ_e is the electron's gyromagnetic ratio ($2\pi \times 2.8$ MHz/Oe) [53]. From the slope of the above relationship, we find that the Gilbert damping constant α is 0.038 ± 0.005 at $T = 258$ K. This α is substantially lower than the recently reported value of 0.28 in thinner FeGe films in an OOP magnetic field applied along the [111] orientation and at unreported temperature [51].

We attribute the second resonance to a helical resonance, also known as the helimagnon. As we point out by a vertical arrow in Fig. 4(c), the helical resonance has a narrow field range (400–500 Oe) but a wide frequency range (4–5.5 GHz), in contrast to the field-polarized phase. We identify this experimental feature to the $n = 4$ helical spin wave resonance that we described in the second region of the micromagnetic simulation that appeared at $f = 4.5$ GHz with four nodes [Fig. 3(c)]. The wavelength of the 4.5 GHz spin wave matches to the helical period of the FeGe film ($2L_D < 176$ nm $< 3L_D$), which supports our interpretation that spin waves are explicitly filtered by the helical spin texture in B20 thin films based on the micromagnetic analysis in Sec. III.

Next, we plot the linecuts at $T = 258$ K for different frequencies [Fig. 4(d)] and at 5.0 GHz frequency for different temperatures [Fig. 4(e)]. In these linecuts, we fit the helical resonance with a derivative of Lorentzian shape as before. At $T = 258$ K between 4.5 GHz and 5.5 GHz frequencies, we can fit the helical resonances separately from the Kittel-type uniform mode, as shown by the red curves in Fig. 4(d). However, at lower frequencies, the uniform mode overlaps strongly with the helical resonance, which makes separate fitting unsuccessful. In Fig. 4(e), we plot $f = 5$ GHz MAS linecuts at different temperatures. While the uniform mode alone is an excellent fit to the MAS data above the critical temperatures ($T = 275$ K), at lower temperatures we clearly observe the emergence of a second helical absorption line between 400 and 500 Oe.

In Fig. 4(f), we plot MAS as a function of magnetic field and temperature at a constant frequency of 4.25 GHz. The helical absorption feature can be seen at both positive and negative magnetic fields, marked by two arrows. Although the field-polarized resonances extend to $T = 280$ K, the helical resonances disappear above $T = 270$ K, close to the critical temperature of FeGe.

Between $T = 270$ K and 280 K, FeGe transitions from the paramagnetic state into the field polarized state–ferromagnetic phase. This region may include a precursor region at low fields, which has a complicated magnetic structure and does not show any resonance feature at low fields. Previously, Wilhelm *et al.* found this precursor region at higher temperatures, between 278 K and 280 K, via magnetic susceptibility measurements of the bulk FeGe [12]. However, from the magnetic susceptibility measurements [Fig. 2(d)], we find a critical temperature 273 K for the helical order, which is lower than the bulk crystal value of 278.2 K. Furthermore, Wilhelm *et al.* observed a skyrmion phase only between $T = 273$ K and 278 K [12], which lies above the helical ordering temperature in our films. Therefore, an open question for thin-film chiral magnets exists: Does the skyrmion phase shift to lower temperature or totally disappear under an IP magnetic field? In contrast, a recent Lorentz-TEM study showed that a confinement of free-standing films along the applied field induces a strong surface twist effect in addition to the exchange, DM, and anisotropy fields, which stabilizes skyrmion formation at wider range magnetic fields and temperatures [54]. This suggests that the IP and OOP fields create substantially different magnetic phases in thin films, which is a point that needs further investigation.

We note that our micromagnetic simulation predicts the $n = 4$ helical spin wave resonance in a relatively narrow frequency range but over wide field range, in contrast to the experimental findings. We attribute this difference to the generic shortcomings of the micromagnetic simulations. First, because we perform a $T = 0$ K simulation, we initialized the magnetic state, thus the simulation does not account for magnetic phase transitions or mixed magnetic states, as mentioned above. Second, we used an artificially low $\alpha = 0.002$ Gilbert damping parameter, which is 19 times smaller than the experimental value $\alpha = 0.038$. Third, the simulations do not account for frequency broadening due to thickness variations. By performing separate calculations, we found that a 5% thickness variation yields 0.5 GHz broadening (see Fig. 5 and the Supplemental Material [36]). We also expect that inhomogeneities in anisotropies and grains increase frequency broadening in the experimental MAS, which will be discussed in the next section with additional simulations and theoretical calculations. Moreover, our MAS experiment does not show any clear resonance peak for $n = 2$ mode spin waves around 2.5 GHz, which was shown in Fig. 3(a) by micromagnetic simulations. Therefore, while micromagnetic calculations remain powerful tools for understanding helical dynamics, the disorder present in real thin-film materials are not perfectly accounted for in our calculations.

Another notable difference between our MAS measurements and our simulation, and contrary to observations by Schwarze *et al.* in bulk B20 materials [33], we do not observe microwave absorption at fields below 400 Oe. This difference may arise from the low-field magnetic disorder imposed by inhomogeneous local strain associated with grains in our films and that we do not account for in micromagnetic simulations. We speculate that grain twinning introduces heterogeneity and that a distribution of states with a varying number of turns washes out the resonance at low fields. Larger fields, however, may help unify the collective magnetic state, enabling a strong helical state resonance absorption before untwisting into the field-polarized state.

VI. THEORETICAL CALCULATIONS

By comparing the micromagnetic simulations and experimental measurements of MAS, we identified the resonance frequencies and spin-wave modes in the helical and field-polarized states. In this section, we also analytically model

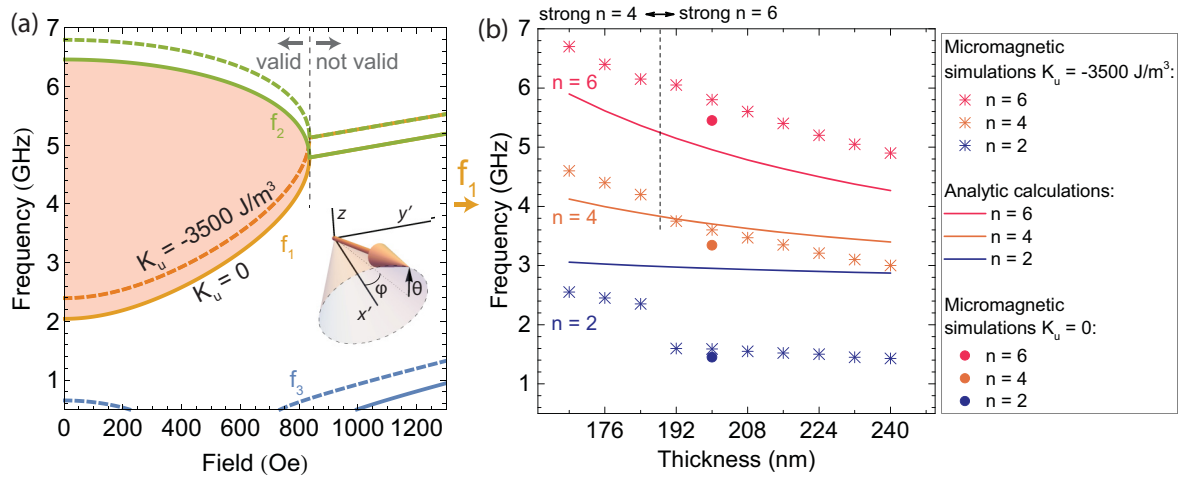

FIG. 5. Analytical calculation of the resonance frequencies for the infinitely thick helical phase (a) and comparison of analytic calculations with micromagnetic simulations (b). (a) The real parts of the eigenvalues of the equations of motion result in three resonance frequencies f_1, f_2, and f_3. The solid and dashed lines show zero anisotropy and nonzero anisotropy calculation results, respectively. The inset shows the coordinate system and angle variables of spins. Because of nonzero imaginary parts of the eigenvalues, only the pink-filled region represents correct resonance feature. (b) Solid lines are analytic calculations (f_1) with additional Kittel's dispersion factor for the film thickness, and the stars are from a micromagnetic simulation for the same film thicknesses. $n = 6$, 4, and 2 represent the number of nodes of spin waves, which are only even numbers because of the applied field (250 Oe) in the x direction. The filled circles are micromagnetic simulations with zero anisotropy for 200-nm-thick film. While the $n = 4$ node spin wave is stronger in the films thinner than 188 nm, $n = 6$ is stronger in the thicker films due to a better match to the helical vector.

excited chiral helimagnets to account for spin wave excitations. Our analytic model consists of two steps to find a thin-film limit solution. (1) We treat the helical state excitations by assuming a fixed helical period but infinitely thick sample, which correctly predicts the bulk helical resonances. (2) An analogy to Kittel's mode described by the magnon dispersion $\hbar\omega = \hbar\omega_{fmr} + D_s q^2$, where $\hbar$ is Planck's constant, D_s is the exchange stiffness, and q is the spin wave vector.

For the first part, we describe the one-dimensional Hamiltonian density of a chiral helimagnet by

$$\mathcal{H} = A(\partial_z \boldsymbol{m})^2 - \boldsymbol{D}.\boldsymbol{m} \times \partial_z \boldsymbol{m} - \boldsymbol{H}.\boldsymbol{m} - K_u(\boldsymbol{m}.\hat{\boldsymbol{n}})^2 - \tfrac{1}{2}\boldsymbol{H_m}.\boldsymbol{m}, \quad (1)$$

where A is the exchange stiffness constant, $\boldsymbol{D}$ is the DM interaction constant, $\boldsymbol{H}$ is the external magnetic field, K_u is the anisotropy constant, and $\boldsymbol{H_m}$ is the demagnetizing field due to shape of the sample. We use the normalized magnetization $m = [\sin\theta(z,t)\cos\phi(z,t), \sin\theta(z,t)\sin\phi(z,t), \cos\theta(z,t)]$ in the spherical coordinate, as in the previous section [21,34,55]. The external magnetic field $\boldsymbol{H}$ includes the dc field H_x and the ac microwave field H_y, written as $\boldsymbol{H} = [H_x, H_y \sin\omega t, 0]$. Next, we write down the Lagrangian density $\mathcal{L}$,

$$\mathcal{L} = -\frac{\hbar M_s}{g_e \mu_B}(\cos\theta - 1)\partial_t\phi - \mathcal{H}, \quad (2)$$

where M_s is the saturation magnetization, μ_B is the Bohr magnetron, and g_e is the electron g-factor. The equations of motion are constructed by expressing Eqs. 1 and 2 in terms of $\theta(z,t)$ and $\phi(z,t)$ coordinates (see the Supplemental Material [36]).

For the equilibrium helical state at $\boldsymbol{H} = 0$, the solutions are simply $\theta = \frac{\pi}{2}$ and $\phi = Qz$, where $Q = \frac{D}{2A}$ is the helix wave number. Application of an external magnetic field creates a deviation from equilibrium by θ_1 and ϕ_1 as

$$\phi(z,t) = Qz + \phi_1(z)\sin\omega t, \quad (3)$$

$$\theta(z,t) = \frac{\pi}{2} + \theta_1(z)\cos\omega t. \quad (4)$$

The distorted helix has been described by cosine expansions of the angles, as in $\phi_1(z)[\theta_1(z)] = A_1[B_1] + A_2[B_2]\cos Qz + A_3[B_3]\cos^2 Qz$, where A_{1-3} and B_{1-3} are coefficients for ϕ_1 and θ_1, respectively [19,21,34,56]. As the last step, we substitute Eqs. 3 and 4 into the equations of motion using the small angle approximation (see the Supplemental Material [36]). We use the same material parameters obtained in the micromagnetic simulation section. Finally, we solve the eigenvalue problem for the resonance frequencies and modes.

In Fig. 5(a), we plot the real part of the three resonance frequencies f_1, f_2, and f_3 as functions of the IP field H_x. Solid curves are calculated assuming zero uniaxial anisotropy, whereas the dashed curves are calculated using a uniaxial anisotropy of $K_u = -3.5\,\mathrm{kJ/m^3}$. If we define a critical field $H_c = 830$ Oe, where the solutions to f_1 and f_2 become degenerate [Fig. 5(a)], then $\mathrm{Im}[f_1] = \mathrm{Im}[f_2] = 0$ and $\mathrm{Im}[f_3] \neq 0$, for $H < H_c$, whereas $\mathrm{Im}[f_1] \neq \mathrm{Im}[f_2] \neq 0$ and $\mathrm{Im}[f_3] = 0$ for $H > H_c$ (see the Supplemental Material [36]). Therefore, the solutions to f_1 and f_2 above H_c do not support natural oscillations. Additionally, the small angle approximation and series expansion are valid only at the low field [in the pink-filled region of Fig. 5(a)] because the phase change from the helical into the field-polarized state happens below the saturation field $H_d = 730$ Oe (Fig. 2).

At $H_x = 0$ and $K_u = 0$, the resonance frequencies become $f_1 = \frac{g_e H_d \mu_b}{2\pi\hbar}$ and $f_2 = \frac{\sqrt{10} g_e H_d \mu_b}{2\pi\hbar}$. For example, Schwarze *et al.*

found resonance frequencies 17 GHz, 4 GHz, and 2 GHz for bulk MnSi, FeCoSi, and Cu_2OSeO_3, respectively [33]. The critical fields were also reported as 6000, 1500, and 800 Oe in table 1 of Ref. [33]. From the $f_1 = \frac{g_e H_d \mu_b}{2\pi\hbar}$ formula, we estimate $f_1 = 16.8$ GHz, 4.2 GHz, and 2.2 GHz for each material, respectively, which is in close agreement with their observations. This relation to the critical field also coincides with the recently developed microscopic theory of spin waves in cubic magnets with DMI by Maleyev [57]. He found that the spin-wave stiffness $D_{sw} = \frac{g_e \mu_B H_d}{Q^2}$, which we calculate is 0.105 eV Å^2 for our FeGe thin film. This value is in agreement with the recent neutron scattering experiment on bulk FeGe at 250 K [58]. Therefore, the first part of our theoretical approach provides a straightforward estimate of helimagnon frequencies in bulk B20 materials.

To obtain the frequencies for a thin-film, chiral magnet spin wave mode, we account for the thickness using the spin wave dispersion, $f = f_{heli} + \frac{D_{sw}}{h}(\frac{\pi n}{L})^2$, where h is Planck's constant, L is the thickness, n is the mode number, and f_{heli} is the bulk helical resonance calculated above. Using $f_1 = 2.4$ GHz for f_{heli} [Fig. 5(a), dashed orange curve], we find the spin wave frequency $f = 2.4 + n^2 0.081$ GHz. Near $H = 0$ where the magnetic state supports odd spin wave modes, we find spin wave frequencies of 3.1 GHz and 4.4 GHz for $n = 3$ and $n = 5$, respectively. These frequencies are close to the ones we predicted via the micromagnetic simulations [Fig. 3(d)]. At $H = 400$ Oe, f_1 becomes 3 GHz, and we find that the $n = 4$ spin wave mode frequency is 4.3 GHz, which is also in good agreement with both the micromagnetic simulation and the experimental findings.

To validate the dispersion of the resonance frequency predicted in our analytical model, we also performed micromagnetic simulations in which we vary the thickness of the film at $H = 250$ Oe field while holding all the other material parameters constant. In Fig. 5(b), we plot the resonance frequencies determined from micromagnetic simulations with stars and the analytic formula with solid lines for $n = 6, 4$, and 2 modes. An IP applied magnetic field aligns the spins at the two surfaces along its direction, allowing only even modes. While we have a small offset between the micromagnetic simulation and the analytic model for $n = 2$ and 6, the $n = 4$ spin wave frequencies correspond well. The small differences in the other two modes may originate from variations in the material parameters (e.g., saturation field, magnetization, and uniaxial anisotropy), which are sensitive to temperature for those temperatures near the critical temperature as studied here. In addition, we calculate the resonance frequencies without the easy plane anisotropy by micromagnetic simulations [Fig. 5(b), filled circles] to show the similar difference found in the analytic calculation [Fig. 5(a)].

Our analytic calculation confirms the increase of the resonance frequency by application of a larger magnetic field, in agreement with micromagnetic simulations [Fig. 3(a)]. On the other hand, Schwarze *et al.* [33] observed the opposite trend in bulk B20, i.e., the larger the field, the smaller the frequency. An important difference between these works, however, is that in our films the magnetic field untwists the helix, while in bulk crystals the magnetic field introduces a conical angle to the helical phase. Therefore, an opposite dependence to the magnetic field is consistent with our theoretical understanding. Similarly, Kishine and Ovchinnikov investigated theoretically the unwrapping of infinitely long helicoids by an IP magnetic field and also reported the opposite frequency vs the field trend than what we report [59]. In this case, the difference arises because Kishine *et al.* [59] considered a continuously varied helicoid period L_D as a function of applied field, whereas we consider the thin-film limit in which the helicoid period is nearly constant over some ranges of field, in agreement with micromagnetic calculation. Although our analytic method and micromagnetic simulations explain many important dynamics in helices and the effects of uniaxial anisotropy and film thickness on these dynamics, full understanding of spin waves in confined chiral magnets will require further theoretical study.

VII. DISCUSSION AND CONCLUSION

Although the application of chiral magnetic materials to technology remains a goal for the future, our theoretical and experimental results establish a framework for understanding the excitations of chiral magnetic states. Additionally, dynamical properties will play a crucial role in information storage technologies based on the spin-torque manipulation of magnetic skyrmions in these materials [7,60–64] and in other applications such as spin-torque oscillators using chiral magnetic materials [65,66]. Also relevant to these applications, we demonstrate that the magnetic damping coefficient in B20 FeGe is 0.038, much smaller than previously reported [51]. This is good news for low-power dynamical devices based on chiral magnetism [67].

Our focus on chiral magnetic dynamics and their correlation with detailed characterization of B20 FeGe grown on a Si substrate is aimed at acquiring the understanding necessary for scalable applications. While pioneering studies of chiral magnetism in bulk, single-crystal samples [7,33,68] have set the stage for chiral spintronics, its practical development will likely require integration with other materials on a substrate. Furthermore, as discussed above, the magnetic properties of thin-film B20 materials are modified by substrate-induced strain, which has a corresponding impact on equilibrium spin textures. Therefore, the development of chiral spintronics is aided by continued study of growth and dynamics of thin-film B20 materials.

To conclude, we present a comprehensive experimental and theoretical study of the microwave resonance dynamics in a chiral magnetic FeGe thin film. We grew FeGe films by magnetron sputtering, and we systematically characterized their physical and magnetic properties. Our films are polycrystalline but have high-quality B20 crystal phase, confirmed by the EBSD. Below the critical temperature, static magnetometry measurements show that the film has a helical to field-polarized magnetic phase transition in the range of 380–500 Oe under an IP magnetic field. Our microwave absorption measurements below the critical temperature also show resonance features for the helical and field-polarized states. By comparing experimental measurements with micromagnetic simulations and analytic calculations, we demonstrate that the helical state has resonant microwave dynamics that are highly sensitive to the twisting spin texture. Our analytical calculations also show that the resonance frequencies strongly depend on the critical saturation magnetic field. By introducing the uniaxial

anisotropy and thickness effect on the magnon dispersion, we achieved a good agreement with the resonance frequencies found by the micromagnetic simulations and the MAS experiment. These results pave the way toward understanding spin wave dynamics in chiral and topological spin textures, grown as thin films without any limitation to scalability, thus promising for an integration of chiral spintronics.

ACKNOWLEDGMENTS

This paper was supported by the Department of Energy Office of Science (Grant No. DE-SC0012245). We also acknowledge the use of facilities of the Cornell Center for Materials Research (CCMR), a National Science Foundation (NSF) Materials Research Science and Engineering Center (MRSEC; Grant No. DMR-1120296), and CCMR research support for K.N. and D.A.M., who collaborated on TEM measurements. We further acknowledge facility use at the Cornell NanoScale Facility, a member of the National Nanotechnology Coordinated Infrastructure (NNCI), which is supported by the National Science Foundation (Grant No. ECCS-1542081). We thank Robert M. Hovden and Lena F. Kourkoutis for valuable discussions and ongoing help with electron microscopy and F. Guo for reviewing the manuscript.

[1] A. Fert, V. Cros, and J. Sampaio, Nat. Nanotechnol. **8**, 152 (2013).
[2] S. Emori, U. Bauer, S. Ahn, E. Martinez, and G. S. D. Beach, Nat. Mater. **12**, 611 (2013).
[3] I. Dzyaloshinsky, J. Phys. Chem. Solids **4**, 241 (1958).
[4] M. L. Plumer and M. B. Walker, J. Phys. C Solid State Phys. **14**, 4689 (1981).
[5] A. Fert, Mater. Sci. Forum **59-60**, 439 (1991).
[6] U. K. Rössler, A. N. Bogdanov, and C. Pfleiderer, Nature **442**, 797 (2006).
[7] N. Nagaosa and Y. Tokura, Nat. Nanotechnol. **8**, 899 (2013).
[8] G. A. Valkovskiy, E. V Altynbaev, M. D. Kuchugura, E. G. Yashina, V. A. Dyadkin, A. V Tsvyashchenko, V. A. Sidorov, L. N. Fomicheva, M. Bykov, E. Bykova, L. Dubrovinsky, and S. V Grigoriev, J. Phys.: Condens. Matter **28**, 375401 (2016).
[9] A. E. Petrova, V. N. Krasnorussky, A. A. Shikov, W. M. Yuhasz, T. A. Lograsso, J. C. Lashley, and S. M. Stishov, Phys. Rev. B **82**, 155124 (2010).
[10] S. M. Stishov, A. E. Petrova, S. Khasanov, G. K. Panova, A. A. Shikov, J. C. Lashley, D. Wu, and T. A. Lograsso, J. Exp. Theor. Phys. **106**, 888 (2008).
[11] K. Shibata, X. Z. Yu, T. Hara, D. Morikawa, N. Kanazawa, K. Kimoto, S. Ishiwata, Y. Matsui, and Y. Tokura, Nat. Nanotechnol. **8**, 723 (2013).
[12] H. Wilhelm, M. Baenitz, M. Schmidt, U. K. Rößler, A. A. Leonov, and A. N. Bogdanov, Phys. Rev. Lett. **107**, 127203 (2011).
[13] N. A. Porter, J. C. Gartside, and C. H. Marrows, Phys. Rev. B **90**, 024403 (2014).
[14] S. X. Huang and C. L. Chien, Phys. Rev. Lett. **108**, 267201 (2012).
[15] M. N. Wilson, E. A. Karhu, A. S. Quigley, U. K. Rößler, A. B. Butenko, A. N. Bogdanov, M. D. Robertson, and T. L. Monchesky, Phys. Rev. B **86**, 144420 (2012).
[16] P. Sinha, N. A. Porter, and C. H. Marrows, Phys. Rev. B **89**, 134426 (2014).
[17] M. Beg, R. Carey, W. Wang, D. Cortés-Ortuño, M. Vousden, M.-A. Bisotti, M. Albert, D. Chernyshenko, O. Hovorka, R. L. Stamps, and H. Fangohr, Sci. Rep. **5**, 17137 (2015).
[18] M. Vousden, M. Albert, M. Beg, M.-A. Bisotti, R. Carey, D. Chernyshenko, D. Cortés-Ortuño, W. Wang, O. Hovorka, C. H. Marrows, and H. Fangohr, Appl. Phys. Lett. **108**, 132406 (2016).
[19] N. A. Porter, C. S. Spencer, R. C. Temple, C. J. Kinane, T. R. Charlton, S. Langridge, and C. H. Marrows, Phys. Rev. B **92**, 144402 (2015).
[20] N. Kanazawa, M. Kubota, A. Tsukazaki, Y. Kozuka, K. S. Takahashi, M. Kawasaki, M. Ichikawa, F. Kagawa, and Y. Tokura, Phys. Rev. B **91**, 041122(R) (2015).
[21] M. N. Wilson, E. A. Karhu, D. P. Lake, A. S. Quigley, S. Meynell, A. N. Bogdanov, H. Fritzsche, U. K. Rößler, and T. L. Monchesky, Phys. Rev. B **88**, 214420 (2013).
[22] M. Kugler, G. Brandl, J. Waizner, M. Janoschek, R. Georgii, A. Bauer, K. Seemann, A. Rosch, C. Pfleiderer, P. Boni, and M. Garst, Phys. Rev. Lett. **115**, 097203 (2015).
[23] J. C. Gallagher, K. Y. Meng, J. T. Brangham, H. L. Wang, B. D. Esser, D. W. McComb, and F. Y. Yang, Phys. Rev. Lett. **118**, 027201 (2017).
[24] M. N. Wilson, A. B. Butenko, A. N. Bogdanov, and T. L. Monchesky, Phys. Rev. B **89**, 094411 (2014).
[25] T. L. Monchesky, J. C. Loudon, M. D. Robertson, and A. N. Bogdanov, Phys. Rev. Lett. **112**, 059701 (2014).
[26] S. A. Meynell, M. N. Wilson, J. C. Loudon, A. Spitzig, F. N. Rybakov, M. B. Johnson, and T. L. Monchesky, Phys. Rev. B **90**, 224419 (2014).
[27] C. Kittel, Phys. Rev. **73**, 155 (1948).
[28] C. Herring and C. Kittel, Phys. Rev. **81**, 869 (1951).
[29] E. B. Myers, D. C. Ralph, J. A. Katine, R. N. Louie, and R. A. Buhrman, Science **285**, 867 (1999).
[30] A. Brataas, A. D. Kent, and H. Ohno, Nat. Mater. **11**, 372 (2012).
[31] H. T. Nembach, J. M. Shaw, C. T. Boone, and T. J. Silva, Phys. Rev. Lett. **110**, 117201 (2013).
[32] A. A. Tulapurkar, Y. Suzuki, A. A. H. Kubota, H. Maehara, K. Tsunekawa, D. D. Djayaprawira, N. Watanabe, and S. Yuasa, Nature **438**, 339 (2005).
[33] T. Schwarze, J. Waizner, M. Garst, A. Bauer, I. Stasinopoulos, H. Berger, C. Pfleiderer, and D. Grundler, Nat. Mater. **14**, 478 (2015).
[34] J. I. Kishine, I. G. Bostrem, A. S. Ovchinnikov, and V. E. Sinitsyn, Phys. Rev. B **86**, 214426 (2012).
[35] J. I. Kishine, I. Proskurin, I. G. Bostrem, A. S. Ovchinnikov, and V. E. Sinitsyn, Phys. Rev. B **93**, 054403 (2016).
[36] See Supplemental Material at http://link.aps.org/supplemental/10.1103/PhysRevB.95.134416 for further physical and magnetic characterization, stress calculations, details of the micromagnetic simulations, additional MAS measurements, FMR linewidth calculations, and details of the theoretical calculations.
[37] E. Karhu, S. Kahwaji, T. L. Monchesky, C. Parsons, M. D. Robertson, and C. Maunders, Phys. Rev. B **82**, 184417 (2010).

[38] H. Wilhelm, M. Schmidt, R. Cardoso-Gil, U. Burkhardt, M. Hanfland, U. Schwarz, and L. Akselrud, Sci. Technol. Adv. Mater. **8**, 416 (2007).
[39] E. A. Karhu, U. K. Rößler, A. N. Bogdanov, S. Kahwaji, B. J. Kirby, H. Fritzsche, M. D. Robertson, C. F. Majkrzak, and T. L. Monchesky, Phys. Rev. B **85**, 094429 (2012).
[40] M. De Graef and M. E. McHenry, *Structure of Materials: An Introduction to Crystallography, Diffraction, and Symmetry* (Cambridge University Press, Cambridge, UK, 2012).
[41] H. Wilhelm, M. Baenitz, M. Schmidt, C. Naylor, R. Lortz, U. K. Rößler, A. A. Leonov, and A. N. Bogdanov, J. Phys.: Condens. Matter **24**, 294204 (2012).
[42] A. I. Figueroa, S. L. Zhang, A. A. Baker, R. Chalasani, A. Kohn, S. C. Speller, D. Gianolio, C. Pfleiderer, G. van der Laan, and T. Hesjedal, Phys. Rev. B **94**, 174107 (2016).
[43] D. Sander, Rep. Prog. Phys. **62**, 809 (1999).
[44] Y. Nii, T. Nakajima, A. Kikkawa, Y. Yamasaki, K. Ohishi, J. Suzuki, Y. Taguchi, T. Arima, Y. Tokura, and Y. Iwasa, Nat. Commun. **6**, 8539 (2015).
[45] A. Chacon, A. Bauer, T. Adams, F. Rucker, G. Brandl, R. Georgii, M. Garst, and C. Pfleiderer, Phys. Rev. Lett. **115**, 267202 (2015).
[46] X. Z. Yu, N. Kanazawa, Y. Onose, K. Kimoto, W. Z. Zhang, S. Ishiwata, Y. Matsui, and Y. Tokura, Nat. Mater. **10**, 106 (2011).
[47] A. Vansteenkiste, J. Leliaert, M. Dvornik, M. Helsen, F. Garcia-Sanchez, and B. Van Waeyenberge, AIP Adv. **4**, 107133 (2014).
[48] D. Wei, *Micromagnetics and Recording Materials* (Springer Science & Business Media, Berlin, Germany, 2012).
[49] L. Zhang, H. Han, M. Ge, H. Du, C. Jin, W. Wei, J. Fan, C. Zhang, L. Pi, and Y. Zhang, Sci. Rep. **6**, 22397 (2016).
[50] R. D. McMichael and M. D. Stiles, J. Appl. Phys. **97**, 10J901 (2005).
[51] M. Beg, M. Albert, M.-A. Bisotti, D. Cortés-Ortuño, W. Wang, R. Carey, M. Vousden, O. Hovorka, C. Ciccarelli, C. S. Spencer, C. H. Marrows, and H. Fangohr, Phys. Rev. B **95**, 014433 (2017).
[52] Y. Wiemann, J. Simmendinger, C. Clauss, L. Bogani, D. Bothner, D. Koelle, R. Kleiner, M. Dressel, and M. Scheffler, Appl. Phys. Lett. **106**, 193505 (2015).
[53] S. S. Kalarickal, P. Krivosik, M. Wu, C. E. Patton, M. L. Schneider, P. Kabos, T. J. Silva, and J. P. Nibarger, J. Appl. Phys. **99**, 93909 (2006).
[54] A. O. Leonov, Y. Togawa, T. L. Monchesky, A. N. Bogdanov, J. Kishine, Y. Kousaka, M. Miyagawa, T. Koyama, J. Akimitsu, T. Koyama, K. Harada, S. Mori, D. McGrouther, R. Lamb, M. Krajnak, S. McVitie, R. L. Stamps, and K. Inoue, Phys. Rev. Lett. **117**, 087202 (2016).
[55] M. Janoschek, M. Garst, A. Bauer, P. Krautscheid, R. Georgii, P. Boni, and C. Pfleiderer, Phys. Rev. B **87**, 134407 (2013).
[56] Y. Togawa, Y. Kousaka, S. Nishihara, K. Inoue, J. Akimitsu, A. S. Ovchinnikov, and J. Kishine, Phys. Rev. Lett. **111**, 197204 (2013).
[57] S. V. Maleyev, Phys. Rev. B **73**, 174402 (2006).
[58] S. Siegfried, Gatchina: IV Polarized Neutron School (2015).
[59] J. I. Kishine and A. S. Ovchinnikov, Phys. Rev. B **79**, 220405(R) (2009).
[60] J. Iwasaki, M. Mochizuki, and N. Nagaosa, Nat. Commun. **4**, 1463 (2013).
[61] W. Jiang, P. Upadhyaya, W. Zhang, G. Yu, M. B. Jungfleisch, F. Y. Fradin, J. E. Pearson, Y. Tserkovnyak, K. L. Wang, O. Heinonen, S. G. E. te Velthuis, and A. Hoffmann, Science **349**, 283 (2015).
[62] F. Jonietz, S. Mulbauer, C. Pfleiderer, A. Neubauer, W. Munzer, A. Bauer, T. Adams, R. Georgii, P. Boni, R. A. Duine, K. Everschor, M. Garst, and A. Rosch, Science **330**, 1648 (2010).
[63] T. Schulz, R. Ritz, A. Bauer, M. Halder, M. Wagner, C. Franz, C. Pfleiderer, K. Everschor, M. Garst, and A. Rosch, Nat. Phys. **8**, 301 (2012).
[64] J. Sampaio, V. Cros, S. Rohart, A. Thiaville, and A. Fert, Nat. Nanotechnol. **8**, 839 (2013).
[65] F. Garcia-Sanchez, J. Sampaio, N. Reyren, V. Cros, and J.-V. Kim, New J. Phys. **18**, 075011 (2016).
[66] R. H. Liu, W. L. Lim, and S. Urazhdin, Phys. Rev. Lett. **114**, 137201 (2015).
[67] J. Iwasaki, W. Koshibae, and N. Nagaosa, Nano Lett. **14**, 4432 (2014).
[68] Y. Onose, Y. Okamura, S. Seki, S. Ishiwata, and Y. Tokura, Phys. Rev. Lett. **109**, 037603 (2012).